Biomass-based 3D micro-meso-macroporous carbon for hybrid-capacitance characteristics and incredible energy density: Reversible charge transfer of multivalent Mn ions

Authors: Qingwen Fan [ad], Peng Fu [a*], Elliot L. Bennett [c], Chaoyun Song [b*], Yuchun Zhang [a]

[a] College of Agricultural Engineering and Food Science, Shandong University of Technology, Zibo 255000, China.

[b] Department of Engineering, Strand Campus, King's College London, London, WC2R 2LS, United Kingdom.

[c] Department of Chemistry, University of Liverpool, Crown Street, Liverpool, L69 7ZD, United Kingdom.

[d] School of Engineering and Physical Sciences, Heriot-Watt University, Edinburgh EH14 4AS, United Kingdom.

[*]**Correspondence:**

Peng Fu, College of Agricultural Engineering and Food Science, Shandong University of Technology, Zibo 255000, China. E-mail: fupeng@sdut.edu.cn.

Chaoyun Song, Department of Engineering, Strand Campus, King's College London, London, WC2R 2LS, United Kingdom. E-mail: chaoyun.song@kcl.ac.uk

Abstract

To achieve the coordination of energy density and power density, the metal oxide (MnO_2) that induce pseudo-capacitance in 3D porous carbon can build high energy density and specific capacitance at high-power density. Here we have showed the synthetization of a composites (JSPCC-MnO_2) with a specific capacitance of 310.6 F/g, an energy density of 111.8 Wh/kg, and a power density of 223.3 W/kg. The percentage of pseudo-capacitance caused by the element Mn is 23.05%, the pseudo-capacitance process of the JSPCC-MnO_2 has involved reversible charge transfer from Mn (II) to Mn (IV) to achieve high specific capacitance and energy density via multiple charge transfer dynamics. And the 3D micro-meso-macro porous structure has provided the electrolyte sufficient active sites and smooth ion migration channels. Atomic-scale information has been provided by classical molecular dynamics. In polarized states, the non-polar water molecular layer is at a higher energy level, and the electrostatic adsorption force between carbon atom and K ion is higher than the hydrophobic force of carbon. The doping MnO_2 has disturbed the density distribution in the local region, changed the ordered structure, and made the doping sites form defects. Green, affordable and renewable biomass has been used as the precursor achieving the high energy density of the carbon-based electrode.

Keywords: Composite Materials, Graded Porous Carbon, High Energy Density, MnO_2, Molecular Dynamics

1. Introduction

In recent decades, contemporary society has developed quickly, which has led to excessive energy consumption and the depletion of fossil fuels [1]. In addition, it has put the sustainability of human health and life, as well as the environment, water, air, and other significant pollutants, in grave danger [2, 3]. As a result, the progression of renewable, clean energy sources such as solar, wind, nuclear, biomass, etc., is only around the corner [4, 5]. Given that power systems constitute the foundation of contemporary industrial civilization, the clean energy sources stated above should not be used as the input energy in their pure form. Energy conversion and storage technology is an essential and crucial link in the process of transforming energy. Electrochemical energy storage systems are considered as the most efficient and practical technology for some applications, including lithium-ion batteries, supercapacitor, and fuel cell. Supercapacitors are frequently applied in high power applications, resulting from the outstanding power density, efficiency, and cycle stability [6].

Double-layer capacitance and pseudo-capacitance are the two primary categories into which the charge storage mechanism of supercapacitors is split [6]. The reversible adsorption and desorption of electrolyte ions at the interface between the electrode surface and the electrolyte solution produces the double-layer capacitance. A high charge-discharge rate, which results in a higher power density, was characterized the physical process, which involves un-redox. The Faraday electron transfer (redox

reaction) between the electrolyte and ions on the electrode surface or in the bulk phase, whose electrochemical characteristics are approximating that of the battery behavior, which can charge and discharge continuously and determine the energy density of the electrode material, is the basis for the charge storage mechanism of pseudo-capacitors. Carbon-based materials are usually favored for high-performance electrode for supercapacitors due to their variety of benefits, including high specific surface area, superior electron transport characteristics, tunable pore size distribution, and their ability to be heteroatom doped [7]. Biomass feedstocks often come from a variety of species sources and may be seen as a precursor to carbon compounds with unique structures and characteristics [8]. In terms of microstructure, biomass materials possessed an abundance of self-sourced porous hierarchical structures and hetero-atomic species (O, N, S, P, and B, etc.), which can reduce the ion transport distance and produce more active sites while also improving the surface wettability of carbon materials [2]. The higher power density of carbon-based electrode materials is a result of the plentiful porous characteristics, which offer enough active sites for ion adsorption and desorption (mainly double-layer capacitors). On the other hand, this also highlights the extraordinarily poor energy density of carbon-based electrode materials. Since the power density of the supercapacitor must constantly be guaranteed, studies always focus on how to increase the energy density. To boost the energy density of capacitors by using the pseudo-capacitor mechanism, it is significant to produce hybrid electrode materials (double-layer capacitors and pseudo-capacitors) [2, 6, 9].

Nowadays, metal oxides, conductive polymers, and other materials are often employed to provide pseudo-capacitive characteristics [10, 11]. Pseudo-capacitive materials should have multiple oxidation valences in order to offer a broad voltage range and high energy density [12]. Theoretically, manganese has numerous oxidation states (+1, +2, +3, +4, +5, +6, and +7), MnO_2 is consequently regarded as a promising pseudo-capacitive electrode material and is frequently applied in the field of power battery and energy storage [2]. Moreover, MnO_2 is in possession of high theoretical specific capacitance (1100~1380 F/g). Although the actual specific capacitance of MnO_2 was only 100~150 F/g in the early research. On account of the Faraday reaction and redox of nanosized manganese oxides across various valences, newly discovered MnO_2 nanostructured materials have a mass specific capacitance of 250–500 F/g [13, 14]. It is generally known that the MnO_2 has a very varied crystal structure with diverse configurations. MnO_2 crystal structures of various configurations are stacked and blended to form different pore sizes. In electrochemistry, the specific capacitance of a MnO_2 electrode decreases sharply along with the increase of the load. Therefore, the specific capacitance of carbon-based electrode materials can be increased by doping the MnO_2 pseudo-capacitive element into carbon materials.

Therefore, MnO_2 was chosen as a pseudo-capacitive material to be combined with porous carbon derived from biomass to synthesize composites with high mass specific capacitance and energy density with the aim to drastically improve the power density. Furthermore, in order to demonstrate the advantages of this method, the electrochemical

properties of porous carbon prepared by $ZnCl_2$ were compared. The pseudo-capacitive behavior of MnO_2 promotes surface adsorption of electrolyte ions and rapidly reversible redox. In addition, the transport of electrolyte ions is simulated by Molecular dynamics in the charge-discharge process. The developed electrode materials exhibit excellent electrochemical performance and considerable energy storage properties in a three-electrode system using aqueous solutions as electrolytes.

2. Materials and Methods

2.1 Materials

The conductive carbon black (BP2000, CARBOT, American) was pre-dried at 105 °C for 12 h. 60% PTFE (D21C, DAIKIN, Japan) emulsion was diluted to 10% with deionized water. The nickel foam (Changde Liyuan New Materials Co., Ltd., China) was cut into 18*18 mm^2 rectangular slices, which were then sonicated in anhydrous ethanol for 30 min and dried for 12 h, whose weight is reported as m_1. The chemical reagents used in this experiment are of analytical grade.

2.2 Experimental Methods

2.2.1 Pretreatment of biomass raw materials

The crushed jujube shell (JS, China) was washed repeatedly with deionized water to eliminate impurities. It was immersed in 1.0 M H_2SO_4 for 12 h, and then rinsed with deionized water until neutral. The pretreated jujube shell (PJS) carbon powder was obtained by heating at a rate of 5 °C/min to 400 °C in a tube furnace with nitrogen atmosphere for 2 h.

2.2.2 Preparation of porous carbon composite

PJS was carbonized and activated in one-step by doping metal compounds to prepare Jujube Shell Porous Carbon Composite (JSPCC). In order to improve the pseudo-capacitance, the mixed supercapacitor composite is developed. MnO_2 is preferred as the doping pseudo-capacitive material because it has numerous oxidation states, which is required of the doping element. In addition, the difference was also examined by comparison with an activator ($ZnCl_2$) that is frequently employed in this field. The detailed process is as follows: PJS and metal compounds (MnO_2 or $ZnCl_2$) were mixed in deionized water as a mass ratio of 1:2, and subjected to ultrasonic treatment for 2 h while being stirred, and then dried at 105 °C. The mixture was transferred into a tube furnace with nitrogen gas atmosphere, and the heating procedure was set at 5 °C/min to 1000 °C for 120 min. The resultant mixture is submerged in an excess of 2 M HCl solution and agitated for 8 h to eliminate extra metal compounds and promote porosity. The carbon material is washed to neutral with deionized water, dried at 105 °C, and finally put through 200 mesh sieves. The porous carbon composites were marked as JSPCC-MnO_2 and JSPCC-$ZnCl_2$. In order to emphasize the superiority of the composite performance, the porous carbon material without doping the metal compounds was utilized as the control group, named as JSPCC-Control.

2.3 Electrochemical Measurements

The active substance, conductive carbon black and PTFE (mass ratio 8:1:1) were added into agate mortar along with anhydrous ethanol. Afterwards, the thin carbon film

146 with a guaranteed active load of 5~6 mg/cm^2 was made by a repeatedly folding roller
147 on a glass plate. The dispersion uniformity and bulk density of the composite material
148 can be improved by repeatedly folding and rolling with the intention of lessening the
149 pulverization phenomenon. After drying at 105 °C, the carbon film of 15*15 mm^2 was
150 sliced and coated over the prepared nickel foam for 60 s under the pressure of 20 MPa,
151 and its weight was measured as m_2. Therefore, the weight of the active substance in the
152 electrode is $m = (m_2-m_1) * 80\%$. The prepared electrode plate is designed for testing
153 the three-electrode system.

154 The electrochemical performance of the electrode in the three-electrode system
155 was investigated utilizing the constructed electrode as the working electrode, the
156 platinum electrode as the counter electrode, and the mercury oxide electrode as the
157 reference electrode. 1 M KOH was chosen as the aqueous electrolyte. The cyclic
158 voltammetry (CV) and galvanostatic charge/discharge (GCD) were measured using an
159 electrochemical workstation (PGSTAT 302N, Autolab, Switzerland).

160 In the three-electrode system, the mass specific capacitance (C, F/g) is calculated
161 based on GCD curve,

$$C = \frac{I \cdot \Delta t}{m \cdot \Delta V} \quad (1)$$

162 I: discharge current (A), Δt : discharge time (s), m: the mass of the active
163 substance in a single electrode (g), ΔV : the potential that removes IR drop in the
164 discharge process (V).

165 The energy density (E, Wh/kg) and the power density (P, W/kg) refer to the

following formula respectively:

$$E = \frac{1}{2} \cdot C \cdot \Delta V^2 \frac{1}{3.6} \quad (2)$$

$$P = 1000 \cdot \frac{E}{t} \quad (3)$$

The pseudo-capacitance was measured from the CV curve, whereby the pseudo-capacitance was calculated by fitting two constants (k_1 and k_2) at each potential in accordance with the formulae [15]. In general, the specific capacitance consists of rate independent component k_1 and diffusion effect component k_2 [16]. The peak current of the pseudo-capacitive effect is a function of v ($I_1 = k_1 v$, v is the scan rate, mV/s.). The peak current induced by the diffusion effect varies with $v^{1/2}$($I_2 = k_2 v^{1/2}$).

$$I(V) = k_1 \cdot v + k_2 \cdot v^{1/2} \quad (4)$$

$$I(V) / v^{1/2} = k_1 \cdot v^{1/2} + k_2 \quad (5)$$

2.4 Structural Characterizations

The weightlessness in the N_2 atmosphere was detected using a thermogravimetric analyzer (TG, Nicolet Is10, Neicher, Germany) at the same temperature as in section 2.2. The surface morphology and microstructure of the samples were obtained using a Scanning Electron Microscope (SEM, Quanta 250, FEI, American) performed at 20.0 kV and Transmission Electron Microscope (TEM, Tecnai G^2 F20, FEI, American) equipped with accelerated voltage of 200 kV, which are all equipped with energy dispersive X-ray spectroscopy (EDS, Quanta 250, FEI, American) for the purpose of detecting the element distribution. The X-ray diffraction spectrometer (XRD, XRD-6100, Shimadzu, Japan) scans at 5 °/min in the range of 5 ~ 90° with Cu K_α radiation to

identify the crystal structure. Al K_α is utilized as the excitation source for the X-ray photoelectron spectrometer (XPS, Nexsa, Thermo Fisher, American), which is used to calibrate the valence states and charge distribution of the elements. The defect degree of carbon materials is analyzed by the laser confocal Raman spectrometer (Raman, LabRAM HR Evolution, HORIBA JobinYvon, France) scanning in the range of 100~3000 cm^{-1} at the excitation wavelength of He-Ne laser 633. To further ascertain the bonding state and chemical groups in the 4000-400 cm^{-1} range, porous carbon materials are subjected to the Fourier-transform infrared spectroscopy (FT-IR, ALPHA II, BRUKER, Germany). Nitrogen adsorption-bending analyzer (JW-BK 300C, JWGB, China) is selected to calculate the specific surface area and pore size distribution of porous carbon materials at 77 K. In this work, the classic Molecular Dynamics (MD) process was performed using the open-source package, GROMACS. The simulation system is based on the constant charge method to simulate the charge and discharge process of electrode materials to obtain atomic scale information. The simulation system consists of two identical nanochannels with positive and negative electrodes, which are composed of two segments of carbon nanotubes with diameter of around 25 Å that are separated by carbon spherical cavity with diameter of 50 Å in the middle. Moreover, MnO_2 nanoparticles with diameter of around 5 Å were placed in the nanochannel for comparison. Details can be found in the supplementary materials.

3. Results and Discussion

3.1 Formation mechanism of composite

The synthetic process of several porous carbon materials was addressed according to the results from TG (Fig. S 1). Due to the breakdown of volatile organic components and the fact that the temperature was over 160 °C while the JS was being pre-treated, the thermogravimetric loss persisted until 400 °C (Fig. S 1 a). Both JSPCC-Control and JSPCC-MnO_2 displayed a comparable thermal weightlessness during the carbonization phase, which is sustained across a broad temperature range (300-700 °C). The quick weight loss process of JSPCC-$ZnCl_2$ happened within a small temperature range (500-600 °C), demonstrating how significantly different the carbonization process of JSPCC-$ZnCl_2$ and JSPCC-MnO_2 are from one to another. Because of the solubility and gel-dissolving properties of zinc chloride on cellulose, $ZnCl_2$ can permeate the raw material during the carbonization process. At the same time, additional carbon is retained as a result of the catalytic dehydration of $ZnCl_2$, which results in the release of hydrogen and oxygen as water. Nevertheless, the JSPCC-MnO_2 is accompanied by a multi-valence shift in Mn during the pyrolysis.

$$MnO_2 + C = MnO + CO \quad (6)$$

$$MnO_2 + CO = MnO + CO_2 \quad (7)$$

$$MnO_2 + C = Mn_2O_3 + CO \quad (8)$$

3.2 Electrochemical activity

Fig. 1 a and b artistically illustrate present the synthesis process of Mn-based

carbon composite and the transition process from organic macromolecules to inorganic carbon molecules, as well as the charging and discharging mechanism of Mn-based carbon electrodes. The energy storage process of this composite electrodes mainly includes two categories: double layer capacitor of physical adsorbing and pseudocapacitance provided by redox reaction. Two mechanisms of Mn-assisted charge storage are proposed in the pseudocapacitance process [17]. The first mechanism is that protons (H^+) and/or alkali metal cations (K^+) are embedded into the bulk phase of the composite by reduction reaction and then removed by oxidation reaction; The second one is the adsorption process of cation (K^+) on the surface of the Mn-base composite (Fig. 1 b). This vividly reveals the principle of excellent electrochemical performance of manganese containing composites. Fig. 1 c and d describe the electrochemical properties (mass specific capacitance, energy density and power density) of the porous carbon materials prepared in this study by using MnO_2 as pore-forming agent and inducing pseudo-capacitance, compared with the porous carbon materials prepared by traditional pore-forming agent ($ZnCl_2$). JSPCC-MnO_2 had a mass specific capacitance (310.6 F/g) than is 73% greater than JSPCC-$ZnCl_2$ (179.4 F/g) at the current density of 1 A/g, which is significantly superior than the specific capacitance of the majority of biomass-based porous carbon materials [6]. Meanwhile, the excellent information on the electrochemical properties of JSPCC-MnO_2 are provided in Table 2 compared with that of the latest carbon-based electrodes. It is worth noting that the energy density of the porous carbon composite material JSPCC-MnO_2 was as high as 111.8 Wh/kg at 1

241 A/g, which is greatly higher than that of traditional carbon-based capacitors [18]. Even
242 porous organic polymers are significantly less energy density than JSPCC-MnO_2 [19].
243 On account of that the specific capacitance mechanism offered by carbon-based
244 materials is primarily the double-layer capacitance formed by ion-diffusion, the energy
245 storage in the form of physical adsorption exhibits a rapid electron transfer rate, which
246 formed the characteristics of optimal balance between high power density and low
247 energy density of carbon-based capacitors [16, 20]. Carbon materials doped with
248 multivalent valent ions Mn induced pseudo-capacitance characteristics that improve the
249 low energy density. As a typical metal oxide, MnO_2 exhibits the performances of high
250 pseudo-capacitance and wide voltage range. Biomass-based activated carbon was
251 combined with MnO_2 to build nanocomposites via hydrothermal process to achieve a
252 specific capacitance of 340 F/g. Meanwhile, the electrode material is created for
253 growing MnO_2 on the surface of a carbon material doped with nitrogen demonstrate an
254 energy density of 29.24 Wh/kg at a power density of 485 W/kg [21]. Mixed
255 supercapacitor systems generally lose power density while gaining energy density [6,
256 22], and is also inevitable within this study. However, the power density of JSPCC-
257 MnO_2 (223.3 W/kg) is still marginally greater than that of JSPCC-$ZnCl_2$ (195.8 W/kg)
258 at the current density of 1 A/g, demonstrating that the fundamental performance is
259 maintained even with a lower power density. Although the Mn doping improved the
260 pseudo-capacitance of carbon materials, the double-layer capacitance still
261 predominates. The pseudo-capacitance is only 23.05%, as seen in Fig. 2d. Furthermore,

JSPCC-MnO_2 showed a power density of over 1000 W/kg and sustained an energy density of 52.3 Wh/kg at a current density of 5 A/g. Therefore, the current density can be modified to coordinate the energy density and power density to meet the actual requirements.

In a three-electrode system, the electrochemical performances of JSPCC-MnO_2, JSPCC-$ZnCl_2$ and JSPCC-Control electrodes were measured such as CV (Fig. 2 a, b, and c) and GCD (Fig. 2 g, h). Different scanning speeds (5~200 mV/s) were used to examine the CV curves of the JSPCC-MnO_2, JSPCC-$ZnCl_2$, and JSPCC-Control electrodes in the voltage ranges of -1.1~0.5 V, -1.1~0.4 V, and -0.2~0.2 V, respectively (Fig. 2 a, b, and c). It can be concluded that the CV profiles of JSPCC-Control and JSPCC-$ZnCl_2$ are approximately rectangular and generally symmetrical, and no noticeable redox peaks are detected, indicating the dominant electrochemical double-layer capacitance and the limited pseudo-capacitance (Fig. 2 b and c). Even at higher scanning speeds, JSPCC-Control and JSPCC-$ZnCl_2$ electrodes nevertheless maintain an excellent near rectangular shape, especially JSPCC-Control, in that the large pore size distribution, low specific surface area, and smooth charge transfer of JSPCC-Control. The porous carbon material JSPCC-$ZnCl_2$ formed by pore-forming agent is mainly microporous, which prevents electrolyte from smoothly reaching the carbon surface under the condition of high scanning speed [18, 23]. Mn ions contribute to the pseudo-capacitance in the presence of electrochemical double-layer capacitance, which was specifically given by JSPCC-MnO_2 [24]. It can be found that there is an obvious

283 pseudo-capacitance feature (the redox potential peak) in the CV curve of JSPCC-MnO_2.
284 The fundamental near-rectangular shape and the typical hump features of the CV curve
285 are also maintained. These properties are brought about by the double-layer capacitance
286 and the pseudo-capacitance, respectively [25]. The pseudo-capacitive curve (Fig. 2 d)
287 fitted with CV data revealed that the pseudo-capacitance of JSPCC-MnO_2 electrode
288 was indispensable position. The contribution rate of pseudo-capacitance was 23.05 %,
289 which was much higher than that of JSPCC-$ZnCl_2$ (1.76%), which also explained the
290 high energy density of JSPCC-MnO_2 electrode (Fig. 1 c). By analyzing the relationship
291 between the contribution rate of pseudo-capacitance and scanning rate (Fig. 2 f), the
292 contribution rate of pseudo-capacitance steadily rose with the increase of scanning
293 speed, whereas the double-layer capacitance displayed the reverse pattern. This is
294 mostly in that the high scanning rate makes it difficult for electrolyte ions to effectively
295 bond to the surface of carbon materials.

296 The mixed capacitance of the JSPCC-MnO_2 electrode caused the GCD curve to
297 not be symmetrical and approximates linear independence in the charging and
298 discharging process (Fig. 2 g). And its specific capacitance of 310.6 F/g is obtained at
299 1A/g. The GCD curve of the JSPCC-$ZnCl_2$ electrode shows well triangular symmetry
300 and an approximate linear correlation (Fig. 2 h), whose specific capacitance is 179.4
301 F/g at 1A/g, proving its good charge-discharge reversibility. When the current density
302 is 0.5, 1, 2, 5, 8, and 10 A/g, the specific capacitance of JSPCC-MnO_2 electrode is 276.4,
303 310.6, 261.4, 147.2, 172.0, and 156.2 F/g, whereas that of JSPCC-$ZnCl_2$ electrode

corresponds to 227.6, 179.4, 191.0, 170.7, 157.4, and 152.8 F/g (Fig. 1). Particularly, the specific capacitance of JSPCC-MnO_2 is obviously superior to that of JSPCC-$ZnCl_2$, especially at low scanning rate, which results in the low scanning rate, that guarantees Mn ions have sufficient time to undergo redox and contribute to the pseudo-capacitance [26]. The rate performance of JSPCC-MnO_2 is 50.3% at 10 A/g based on the specific capacitance of 1A/g, whereas that of the JSPCC-$ZnCl_2$ reaches 85.2% on account of its double-layer capacitance. The first derivative of voltage (V) versus time (s) during the discharge stage of the GCD curve at 0.5 A/g was determined to further study the intricate mechanism of the pseudo-capacitive (Fig. 2 j and k). For an ideal double-layer capacitor, the voltage and time should be a perfect linear function, meaning that the first derivative of the voltage over time should be constant. Therefore, the pseudo-capacitance behavior of the electrode material can be reflected as mentioned by the fluctuation of the first derivative of the voltage to the time. The capacitive behavior of JSPCC-MnO_2 may be separated into four stages from Fig. 2 j. Phases I, II, and III are obviously generated by the multivalent migration of Mn ions, which results in the change of the corresponding voltage change rate. Consequently, we considered that these three stages as mixed capacitance behaviors (pseudo-capacitance and double-layer capacitance). It has been deduced that the redox within Mn (III) and Mn (IV) is the primary energy storage mechanism [27]. Phase IV was determined to be a single double-layer capacitive behavior because the first derivative of Phase IV voltage is approximately constant. The JSPCC-$ZnCl_2$ discharge process may be split into two

phases depending on the voltage change rate. Phase I was brought on by the redox of the residual Zn ions and double-layer capacitance. The pseudo-capacitance process of Zn ions differs from that of JSPCC-MnO_2 for that Zn ions are metal ions with a single valence. Phase II of the JSPCC-$ZnCl_2$ performed similarly to Phase IV of the JSPCC-MnO_2. According to the fitting results of the pseudo-capacitance parameter (Fig. 2 j andk), the pseudo-capacitance accounted for 23.05 % in JSPCC-MnO_2 and only 1.76 % in JSPCC-$ZnCl_2$, with the pseudo-capacitance caused by multivalent Mn ions being significantly higher than that contributed by monovalent Zn ions. Fig. 2 i reflects the electrochemical impedance spectrum information and equivalent circuit diagram of electrode materials to describe the electron/ion transport process and electrochemical capacitance behavior. In the low frequency region, the imaginary component of the Nyquist curve shows a sharp upward trend indicating the low ion diffusion resistance [18]. At high frequencies, both JSPCC-MnO_2 and JSPCC-$ZnCl_2$ exhibit low ohmic resistance (<1 Ω). JSPCC-MnO_2 shows a rapid rise in the imaginary component at higher frequencies than JSPCC-$ZnCl_2$, indicating a faster ion diffusion rate and improved chemical kinetics [28]. The two composites (JSPCC-MnO_2 and JSPCC-$ZnCl_2$) were assembled as symmetrical capacitor devices to test the cyclic stability (Fig. 2 l), showing consistent traces of cyclic stability. The retention rate of specific capacitance fluctuates in a narrow range. After 10000 cycles, the specific capacitance retention rate is still above 99%. Therefore, MnO_2 is an excellent substance to induce pseudo-capacitance.

3.3 Morphological and structural characterization

The surface morphology and microstructure of raw materials and porous carbon composites were recorded by SEM and TEM (Fig. 3 and Fig. 4). According to SEM, the JS has a large granular and comparatively round edges, and following processing, the surface morphology shifts to a relatively flat and sharp edge (Fig. 3 a and Fig. S 2 a). The surface morphology from the pretreatment step is mostly retained during the carbonization process (Fig. 3 b, c, and e). JSPCC-MnO_2 shown relatively regular distribution in the size of the particles due to the actions of MnO_2, while the JSPCC-$ZnCl_2$ and JSPCC-Control exhibit the contrary. It is found that there are significant amounts of C and O elements and relatively little N element on the carbon surface from EDS distribution overview (Fig. S 3). The distribution of Mn and Zn on the surface of JSPCC-MnO_2 and JSPCC-$ZnCl_2$, respectively, is observed (Fig. 3 d and f). And the distribution density of Mn is significantly greater than that of Zn indicating that abundant Mn can fully induce pseudo-capacitance, which is consistent with the ratio of pseudo-capacitance of JSPCC-MnO_2 composite being higher than that of JSPCC-$ZnCl_2$ (Fig. 2). The nano-scale structure information was obtained by TEM to further observe the microstructure of porous carbon composites (Fig. 4, and Fig. S 2 b). After processing, the pore structure of JS progressively changed from being flatter to being denser at the nanoscale (Fig. 4 a, Fig. 5 b and Fig. S 2 b). The structure of JSPCC-Control is comparable to that of the PJS, indicating that the JS does not spontaneously transform into a porous structure at high temperatures. The porous structure, notably in

JSPCC-$ZnCl_2$, can be improved by active pore-forming agents, which shows a nano-scale porous structure and interconnected pores (Fig. 4 d), providing sufficient physical conditions for the excellent double layer capacitance of JSPCC-$ZnCl_2$ electrode. Although the sufficient porosity of JSPCC-$ZnCl_2$ is not found in TEM image of JSPCC-MnO_2, the detected crystal structure is conducive to improve the conductivity of carbon materials and the rate of charge transfer (Fig. 4 c). We believe that the crystal structure detected in the carbon material is primarily provided by the metal oxides of manganese and a small amount of graphitized carbon, since some researchers have confirmed that MnO_2 carries the effect of reducing the graphite temperature of carbon materials and promoting the conversion of non-fixed carbon to graphitic carbon [2]. A lattice stripe of d = 0.286 nm corresponding to the graphite plane (002) is shown in the high-resolution TEM image (Fig. 4 c). Moreover, the nano grade distribution of doped metal components (Mn and Zn) from TEM images is comparable to that of SEM (Fig. 4 e and f). Therefore, the plentiful Mn element with the characteristics of induced pseudo-capacitance in JSPCC-MnO_2 electrode materials provided a guarantee for excellent energy density.

The pore characteristics of carbon materials were assessed by the nitrogen adsorption-desorption method at 77 K (Fig. 5 and Table 1). Similar adsorption-desorption isotherms (type I) with the H4 of the hysteresis loop were observed for JSPCC-$ZnCl_2$ and JSPCC-MnO_2. The type I isotherm has obvious adsorption inflexion and well-developed adsorption-desorption platform in the low pressure region,

388 indicating abundant micropore structure (Fig. 5 a). Meanwhile, the H4 hysteresis loop
389 matched a narrow fissure hole. However, the greater pore capacity of JSPCC-$ZnCl_2$ is
390 demonstrated by the fact that its adsorption volume is significantly bigger than that of
391 JSPCC-MnO_2. In addition, JSPCC-$ZnCl_2$ exhibited higher specific surface area (1142.0
392 m^2/g) and total pore volume (0.74 cm^3/g) compared with 386.7 m^2/g and 0.25 cm^3/g of
393 JSPCC-MnO_2, which is consistent with the relationship between pore volume and pore
394 size distribution (Fig. 5 b and Table 1). The specific surface area of JSPCC-$ZnCl_2$ is
395 significantly higher than that of JSPCC-MnO_2, which theoretically allow for the
396 provision of more active sites on the electrode. However, the specific capacitance of
397 JSPCC-$ZnCl_2$ shows the reverse trend. This may be due to the fact that the most
398 common pore size of JSPCC-$ZnCl_2$ is smaller than that of JSPCC-MnO_2, and that the
399 narrow pores make it more difficult for electrolyte ions to smoothly reach the pore
400 surface, ultimately resulting in a significant portion of the specific surface area not
401 functioning. Microporous electrode materials result in degraded electrochemical
402 properties, particularly at high current densities, in that narrow pores and intricate pores
403 hinder the transport and storage of electrolyte ions [23].

404 The graphitization and carbon defect degree of porous carbon composites were
405 analyzed by XRD and Raman (Fig. 5 c and d). The XRD patterns of porous carbon
406 composites (JSPCC-Control, JSPCC-MnO_2, and JSPCC-$ZnCl_2$) revealed two broad
407 diffraction peaks at 2 θ values of 24.6° and 44.1°, corresponding to the (002) plane and
408 (101) plane of non-fixed carbon (Fig. 5 c), which implies that porous carbon composite

materials are mainly non-fixed carbon. The JS and PJS samples only showed amorphous carbon in (002) plane, possibly as a result of the high temperature carbonization destroying the amorphous carbon structure in (002) plane and causing the composite to change into amorphous carbon in (101) plane (Fig. 5 c, Fig. S 4 a). The XRD patterns of all the porous carbon composites show a broad diffraction peak denoting a lower degree of graphitization. The graphitizatized structure of porous carbon materials is also illustrated by the Raman spectra (Fig. 5 d and Fig. S 4 b). The main distinctive peaks of three porous carbon composite materials are the D band (1350 cm^{-1}) and G band (1580 cm^{-1}), which, respectively, reflect the defect site or disorderly sp^2 hybrid carbon atom and in-plane oscillations of sp^2-bonded heteroatoms [18]. The relative strength ratio (I_D/I_G) of D-band and G-band is usually used to reflect the graphitization degree or defect degree of porous carbon materials [29]. A lower I_D/I_G values were associated with higher graphitization degree, whereas a higher I_D/I_G value indicated a higher degree of defects. The I_D/I_G values of JSPCC-Control, JSPCC-MnO_2, and JSPCC-$ZnCl_2$ are 3.04, 2.59, and 3.45, respectively, revealing the lower degree of graphite, which was consistent with the results of XRD. The relatively low I_D/I_G value of JSPCC-MnO_2 demonstrated that doping MnO_2 to porous carbon materials can increased the graphitization degree. In addition to the public characteristics peak, JSPCC-MnO_2 shows an exclusive diffraction peak located at 642.8 cm^{-1}. There is a strong linear positive correlation between peak strength and manganese content. The Mn-O vibration and dual-chain vibration formed by Mn-O octagonal are responsible

for the strong peak at 642.8 cm^{-1}, showing the tetragonal structure and high crystallinity, which again prove the successful synthesis of porous carbon composites that induce pseudo-capacitive properties and explain the high energy density of JSPCC-MnO_2 electrode materials. The surface chemical properties of JS and porous carbon composites were analyzed, FT-IR showed the distribution of functional groups on the surface of carbon materials (Fig. S 4 c and Fig. S 5). The number of stretching vibration peaks of JS was more than that of porous carbon materials, which suggested that there were abundant functional groups on the surface of the raw material. The vibration of O-H is responsible for the strong peaks at 3450 cm^{-1} and 1600 cm^{-1}. The peak of JSPCC-MnO_2 at 546 cm^{-1} is attributed to the vibrations of Mn-O.

In order to comprehend the elemental composition and chemical bonding state of porous carbon composites, more thorough information was supplied by XPS (Fig. 5 e ~i). It can be shown that majority of the elements in porous carbon composites, as depicted in Fig. 5 e, are C and O elements. The large fraction of pseudo-capacitance in JSPCC-MnO_2 can be attributed to the Mn element, which was presented in JSPCC-MnO_2 in addition to the C and O components. C 1s XPS spectrum was fitted by Gauss-Lorenz fitting method to provide detailed separated peak information (Fig. 5 f~i and Fig. S 4 d). The peak strength of sp^2-C is plainly higher than that of other C-configurations, which reflects the transition from amorphous carbon to graphitized carbon during carbonization. JSPCC-$ZnCl_2$ shows 6 C-configurations including sp^2-C, sp^3-C, C-O, C=O, O=C-O, and π-π*, whereas JSPCC-MnO_2 material only possesses 4

C-structures type (sp^2-C, sp^3-C, C-O, O = C-O), this may be the cause of their variation. JSPCC-MnO_2 is rich in Mn element, so the same curve fitting method was used to fit the peak of Mn-2p (Fig. 5 i). Three valence states of Mn ions (+2, +3, and +4) can be obtained, and the multi-valence state of Mn element is an important factor in the high pseudo-capacitance of JSPCC-MnO_2. Moreover, the primary process of energy storage is the redox reaction between Mn (III) and Mn (IV) [27], and the abundance of Mn (IV) in JSPCC-MnO_2 is conducive to increase the energy storage capacity of pseudo-capacitor.

3.4 Molecular dynamics simulations

Classical molecular dynamics simulations are performed to analyze the migration process of ions in the zero potential state and polarization state from the atomic scale. Fig. 6 describes the number density distribution of electrolyte ions in a one-dimensional direction (axial direction). It can be found that the anions and cations are evenly distributed in the system regardless of whether MnO_2 is doped or not under zero voltage conditions. Moreover, the number density distribution of OH ions is slightly higher than that of K ions, which may be because the OH ions are supplied by both KOH and water. From the visible distribution of model ions, there is a large gap between the electrolyte ions and the carbon network surface due to the existence of a hydration layer, while the gap between the electrolyte ions and the carbon surface at the activated sites of doping MnO_2 is shortened. Furthermore, the doped MnO_2 perturbs the number density distribution of anions and cations in the doped local regions, that is, the number density

472 increases obviously at the MnO_2-doped sites (Fig. 6 b). The doping of MnO_2 changed
473 the flat and ordered structure of the carbon network and made the doping sites form
474 defect characteristics, which contributed to the increase of ion adsorption [30]. This
475 phenomenon explains from the atomic scale that the specific capacitance of MnO_2
476 composites is higher than that of undoped MnO_2 composites. When the system is
477 polarized, the anions and cations migrate rapidly from the electrolyte to the surface of
478 the electrode, and a large number of anti-ions are accumulated on the surface of the
479 electrode (Fig. 6 b and d). Meanwhile, the anion (OH^-) and carbon surface formed a
480 uniform thickness gap of the hydration layer, mainly because the more orderly
481 arrangement of the non-polar water molecules makes the carbon surface a higher energy
482 level [31]. The cation (K^+) is closely attached to the carbon surface since that the
483 hydrophobic force of the carbon atom is less than the adsorption force of the opposite
484 charge between the carbon atom and K ion. Although MnO_2 particles occupy a certain
485 physical space in the pores, it has no effect on the ion electrostatic adsorption on the
486 carbon surface. Fig. 7 shows the two-dimensional distribution of electrolyte ions in the
487 radial direction. In the zero-voltage state, K and OH ions are uniformly distributed in
488 the two-dimensional direction without MnO_2-doping (Fig. 7 A-b and A-e). MnO_2
489 breaks the consistent distribution of anions and cations, and there are obvious highlights
490 at the doping sites in the radial direction (Fig. 7 B-b and B-e), which indicates that the
491 number density of ions at the doping sites is much higher than that at other places. In
492 the polarized state, K^+ formed distinct bright rings at the negative pole and OH^- at the

positive pole, illustrating the aggregation of hetero-charges (Fig. 7 A-a, A-f, B-a, and B-f). The results are consistent with the one-dimensional density distribution of ions.

The migration process of molecules can be observed intuitively according to the Mean Square Displacement (MSD), MnO_2 does not affect the migration behavior of ions, and the two models show the same ion migration process (Fig. S 9). However, the polarization behavior of the electrode shows an obvious limitation on the migration of ions, especially K^+ and OH^-. Due to the electrostatic interaction, the electrolyte ions are bound to the surface of the carbon material, which limits the range of activity. This also explains the phenomenon of multi-layer anti-ions on the inner surface of the pore in the one-and two-dimensional directions. The diffusion coefficient (Table 3) is obtained from the MSD, and it is observed that K^+ and OH^- have very low diffusion coefficients in the polarized state whether or not doped MnO_2. Doping-MnO_2 at zero potential slightly limits the ion diffusion behavior. The Radial distribution function is used to describe the spatial relationship between atoms and the Order of matter (Fig. 8 and Fig. S 8). According to the RDF of zero potential, C-K, C-OH, and C-water show a short-range disorder state (Fig. 8 b and e). When the electrode is polarized, K^+ is mainly distributed on the surface of the negative electrode. The RDF shows that there is a strong peak of K distribution at near r = 2.975 Å, and with the increase of r, the intensity of g(r) gradually converges to 1. The results show that the K-ion distribution on the negative carbon surface is near-range ordered (Fig. 8 a, d, and g). However, the radial distribution of OH and water molecules on the cathode surface can be ignored. In the

positive electrode, the RDF of C-OH shows two obvious strong peaks near r=2.975 Å and r=5.625 Å as r increases. And C-K presents a short-range disorder (Fig. 8 c, f, and g). The migration process of different ions on the electrode surface is directly related to the capacitive behavior. The atomic behavior process of anions and cations is explained from the microscopic scale by molecular dynamics simulation.

4. Conclusion

3D micro-meso-macro porous carbon was synthesized from jujube shell biomass by thermochemical conversion in inert gas atmosphere. In the synthetic process, doping with metal oxides (MnO_2) can successfully induce the pseudo-capacitance of porous carbon composite to improve the energy density and mass specific capacitance. In the present study, JSPCC-MnO_2 composite was synthesized with the mass specific capacitance of 310.6 F/g and energy density of 111.8 Wh/kg at 1 A/g, even under the power density condition of 223.3 W/kg. The pseudo-capacitance induced by Mn element in JSPCC-MnO_2 composite is 23.05%, and the ratio of pseudo-capacitance ensures the dominant position of the double-layer capacitance, which is beneficial to maintaining the power density of the composite. Moreover, the unique pseudo-capacitance process of the JSPCC-MnO_2 composite involved complete reversible charge transfer from Mn (II) to Mn (IV), which achieves high specific capacitance and energy density via multiple charge transfer dynamics. Additionally, the porous structure, mainly 2 nm in diameter, provides sufficient active sites and smooth ion migration channels for the electrolyte. The molecular dynamics simulation observed that, in the

polarized state, the anions (OH^-) formed a uniform hydrate gap with the carbon surface, while the cations (K^+) were closely attached to the carbon surface, resulting from that the non-polar water molecular layer is at a higher energy level, and the electrostatic adsorption force between carbon atom and K ion is higher than the hydrophobic force of carbon atom. The doping of MnO_2 disturbs the density distribution in the doping local region, changes the flat and ordered structure of the carbon network, and makes the doping sites form defects, which increases the ion adsorption capacity. This method realizes the high energy density of carbon-based electrode materials and promotes the further development of biomass porous carbon electrode materials.

Acknowledgements

This work was financially supported by the National Natural Science Foundation of China [51976112], Special Project Fund of "Taishan Scholar" of Shandong Province [tsqn202103066], Shandong Provincial Natural Science Foundation [ZR2022ME109], and China Scholarship Council [202201040003].

Competing interests

The authors declare no competing interests.

Appendix A. Supporting information

Supplementary data associated with this article can be found in the online version.

553 **References**

554 [1] X. Liu, C.-F. Liu, S. Xu, T. Cheng, S. Wang, W.-Y. Lai, W. Huang, Chemical
555 Society Reviews, 51 (2022) 3181-3225.
556 [2] X. Tang, D. Liu, Y.-J. Wang, L. Cui, A. Ignaszak, Y. Yu, J. Zhang, Progress in
557 Materials Science, 118 (2021) 100770.
558 [3] Q. Fan, X. Fan, P. Fu, Y. Li, Y. Zhao, D. Hua, Bioresource Technology, 347
559 (2022) 126384.
560 [4] R.J. Shi, X.C. Fan, Y. He, Renewable & Sustainable Energy Reviews, 69
561 (2017) 461-471.
562 [5] H. Liu, T. Xu, K. Liu, M. Zhang, W. Liu, H. Li, H. Du, C. Si, Industrial Crops
563 and Products, 165 (2021) 113425.
564 [6] J. Zhao, A.F. Burke, Energy Storage Materials, 36 (2021) 31-55.
565 [7] P. Han, M. Cheng, D. Luo, W. Cui, H. Liu, J. Du, M. Wang, Y. Zhao, L.
566 Chen, C. Zhu, J. Xu, Energy Storage Materials, 24 (2020) 486-494.
567 [8] B. Xue, Z. Wang, Y. Zhu, X. Wang, R. Xiao, Industrial Crops and Products,
568 170 (2021) 113724.
569 [9] Y. Liu, Z. Ge, Z. Li, Y. Chen, Nano Energy, 80 (2021) 105500.
570 [10] F. El-Kady Maher, M. Ihns, M. Li, Y. Hwang Jee, F. Mousavi Mir, L.
571 Chaney, T. Lech Andrew, B. Kaner Richard, Proceedings of the National Academy of
572 Sciences, 112 (2015) 4233-4238.
573 [11] M.R. Lukatskaya, B. Dunn, Y. Gogotsi, Nature Communications, 7 (2016)

574 12647.

575 [12] V. Augustyn, P. Simon, B. Dunn, Energy & Environmental Science, 7

576 (2014) 1597-1614.

577 [13] M. Liu, L. Gan, W. Xiong, Z. Xu, D. Zhu, L. Chen, Journal of Materials

578 Chemistry A, 2 (2014) 2555-2562.

579 [14] S. He, W. Chen, Journal of Power Sources, 294 (2015) 150-158.

580 [15] X.J. Pu, D. Zhao, C.L. Fu, Z.X. Chen, S.N. Cao, C.S. Wang, Y.L. Cao,

581 Angewandte Chemie-International Edition, 60 (2021) 21310-21318.

582 [16] T. Lin, I.W. Chen, F. Liu, C. Yang, H. Bi, F. Xu, F. Huang, Science, 350

583 (2015) 1508-1513.

584 [17] M. Toupin, T. Brousse, D. Bélanger, Chemistry of Materials, 16 (2004)

585 3184-3190.

586 [18] Y. Gong, D. Li, C. Luo, Q. Fu, C. Pan, Green Chemistry, 19 (2017) 4132-

587 4140.

588 [19] J. Li, M. Chen, S. Zhou, H. Li, J. Hao, Chemical Society Reviews, 51

589 (2022) 3226-3242.

590 [20] Z. Zhao, Z. Tang, Y. Zhang, Industrial Crops and Products, 170 (2021)

591 113772.

592 [21] T. Ouyang, K. Cheng, F. Yang, L. Zhou, K. Zhu, K. Ye, G. Wang, D. Cao,

593 Journal of Materials Chemistry A, 5 (2017) 14551-14561.

594 [22] H. Ji, X. Zhao, Z. Qiao, J. Jung, Y. Zhu, Y. Lu, L.L. Zhang, A.H.

595 MacDonald, R.S. Ruoff, Nature Communications, 5 (2014) 3317.

596 [23] X. Zheng, J. Luo, W. Lv, D.-W. Wang, Q.-H. Yang, Advanced Materials, 27

597 (2015) 5388-5395.

598 [24] Y.-T. Weng, H.-A. Pan, R.-C. Lee, T.-Y. Huang, Y. Chu, J.-F. Lee, H.-S.

599 Sheu, N.-L. Wu, Advanced Energy Materials, 5 (2015) 1500772.

600 [25] L.-F. Chen, X.-D. Zhang, H.-W. Liang, M. Kong, Q.-F. Guan, P. Chen, Z.-Y.

601 Wu, S.-H. Yu, ACS Nano, 6 (2012) 7092-7102.

602 [26] J. Li, S. Luo, B. Zhang, J. Lu, W. Liu, Q. Zeng, J. Wan, X. Han, C. Hu,

603 Nano Energy, 79 (2021) 105410.

604 [27] G. Saat, F.M. Balci, E.P. Alsaç, F. Karadas, Ö. Dag, Small, 14 (2018)

605 1870003.

606 [28] H. Huang, X. Chu, Y. Xie, B. Zhang, Z. Wang, Z. Duan, N. Chen, Z. Xu, H.

607 Zhang, W. Yang, ACS Nano, 16 (2022) 3776-3784.

608 [29] S.L.H. Rebelo, A. Guedes, M.E. Szefczyk, A.M. Pereira, J.P. Araújo, C.

609 Freire, Physical Chemistry Chemical Physics, 18 (2016) 12784-12796.

610 [30] Y.-C. Wu, J. Ye, G. Jiang, K. Ni, N. Shu, P.-L. Taberna, Y. Zhu, P. Simon,

611 Angewandte Chemie International Edition, 60 (2021) 13317-13322.

612 [31] W. Zhang, J. Yin, W. Jian, Y. Wu, L. Chen, M. Sun, U. Schwingenschlögl,

613 X. Qiu, H.N. Alshareef, Nano Energy, 103 (2022) 107827.

614 [32] F. Wang, J.Y. Cheong, J. Lee, J. Ahn, G. Duan, H. Chen, Q. Zhang, I.-D.

615 Kim, S. Jiang, Advanced Functional Materials, 31 (2021) 2101077.

[33] X. Gao, X. Du, T.S. Mathis, M. Zhang, X. Wang, J. Shui, Y. Gogotsi, M. Xu, Nature Communications, 11 (2020) 6160.

[34] J. Yan, L. Miao, H. Duan, D. Zhu, Y. Lv, W. Xiong, L. Li, L. Gan, M. Liu, Electrochimica Acta, 358 (2020) 136899.

620 **Table**

621 Table 1 Adsorption parameters of porous carbon composites from N_2 adsorption
622 isotherms.

Index	JSPCC-MnO_2	JSPCC-$ZnCl_2$
Isotherm type	I	I
Hysteresis loop	H4	H4
BET surface area (m^2/g)	386.7	1142.0
t-method external surface area (m^2/g)	67.4	466.8
Total pore volume (cm^3/g)	0.25	0.74
Micropore volume (cm^3/g, D<2 nm)	0.13	0.30
average pore diameter (nm)	2.59	2.58
Most probable pore diameter (nm, dV/dD)	2.29	2.11

623 The related parameters were calculated from the N_2 adsorption isotherms. Pore
624 diameter is calculated by the BJH method.

625

626 Table 2 Comparison of electrochemical performances (specific capacitance (C),

627 energy density (E), and power density (P)).

Electrode	Current Density	C (F/g)	E (Wh/kg)	P (W/kg)	Electrolyte
JSPCC-MnO_2	**1** A/g	**310.6**	**111.8**	**223.3**	**1 M KOH**
Bamboo char [18]	0.5 A/g	222.0	6.68	100.2	6 M KOH
Enzymolysis-Treated Wooden carbon [32]	1-30 mA/cm^2	235-328	10.97	26.33	6 M KOH
MXene-knotted CNT composite[33]	1-20 A/g	130	59	9.6	Organic electrolyte
N/O doping Core-shell porous carbon spheres [34]	0.5-8 A/g	212	31.6	550	6 M KOH

628

629 Table 3 Diffusion coefficient of multi-ions in different states

Category	Potential state	Ions	Linear fitting equation	R^2	Diffusion coefficient (D, $10^{\wedge-5}$ cm^2/s)
Free-MnO_2	Zero-potential	water	y=0.01395x+9.58013	0.999	2.325
		K^+	y=0.00846x+8.21872	0.999	1.41
		OH^-	y=0.00647x+10.21182	0.997	1.078333
	Polarized	water	y=0.00794x+6.04065	0.999	1.323333
		K^+	y=0.00172x+1.60828	0.999	0.286667
		OH^-	y=0.00103x+1.10466	0.999	0.171667
Doping-MnO_2	Zero-potential	water	y=0.01355x+9.03382	0.999	2.258333
		K^+	y=0.00795x+9.71359	0.997	1.325
		OH^-	y=0.00619x+10.6875	0.987	1.031667
	Polarized	water	y=0.00794x+5.9619	0.999	1.323333
		K^+	y=0.00172x+1.58718	0.999	0.286667
		OH^-	y=0.00103x+1.09019	0.998	0.171667

630

631 **Figures**

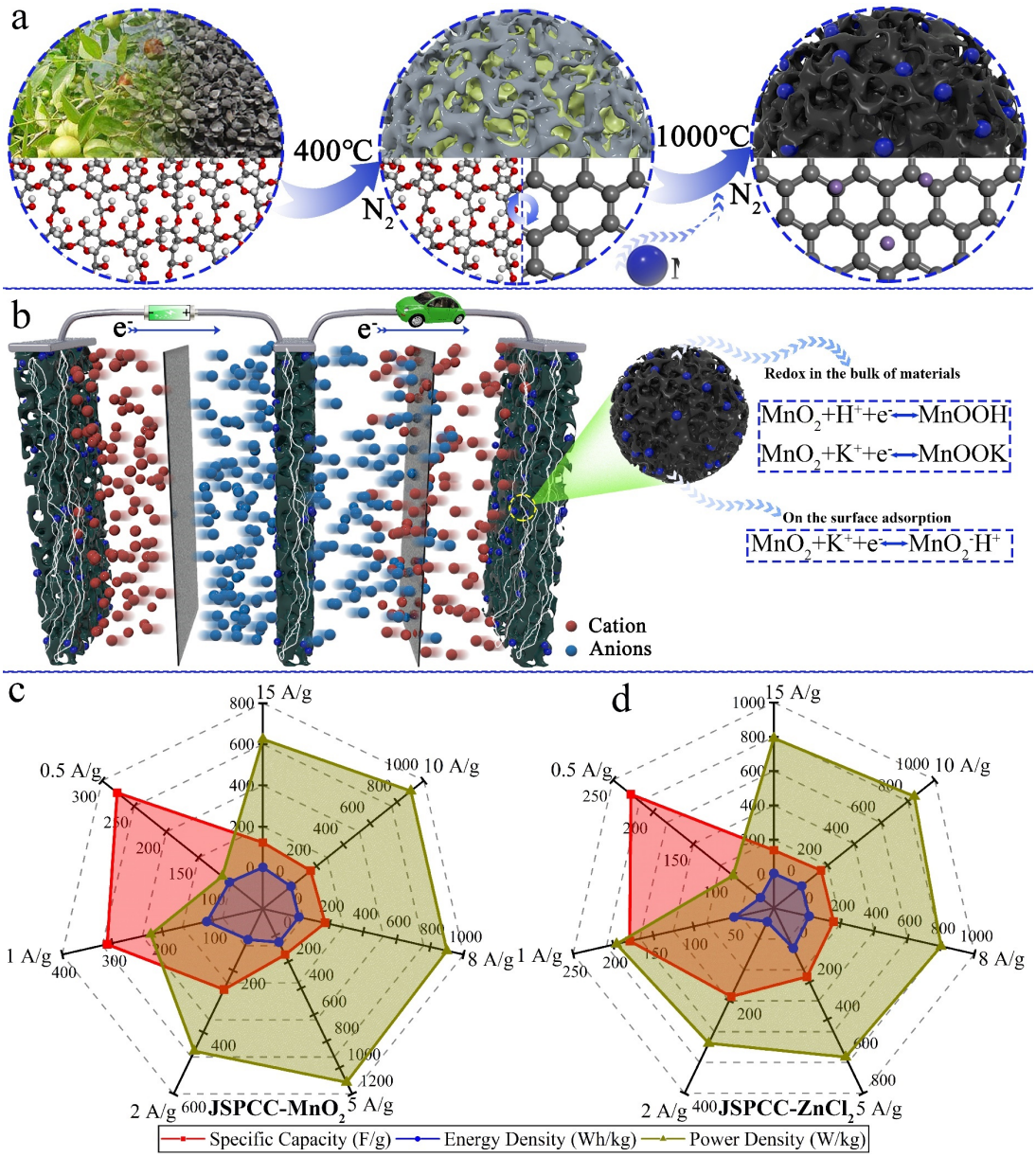

632

633 Fig. 1 Artistic views of the composite material preparation process (a); Schematic
634 illustration of the charge storage processes of Mn-doped carbon-based composite
635 electrodes in a redox (b); and Electrochemical performance parameters (c). The mass
636 specific capacitance (F/g), energy density (Wh/kg) and power density (W/kg) at
637 gradient current density (0.5, 1, 2, 5, 8, 10, and 15 A/g) from GCD curve.

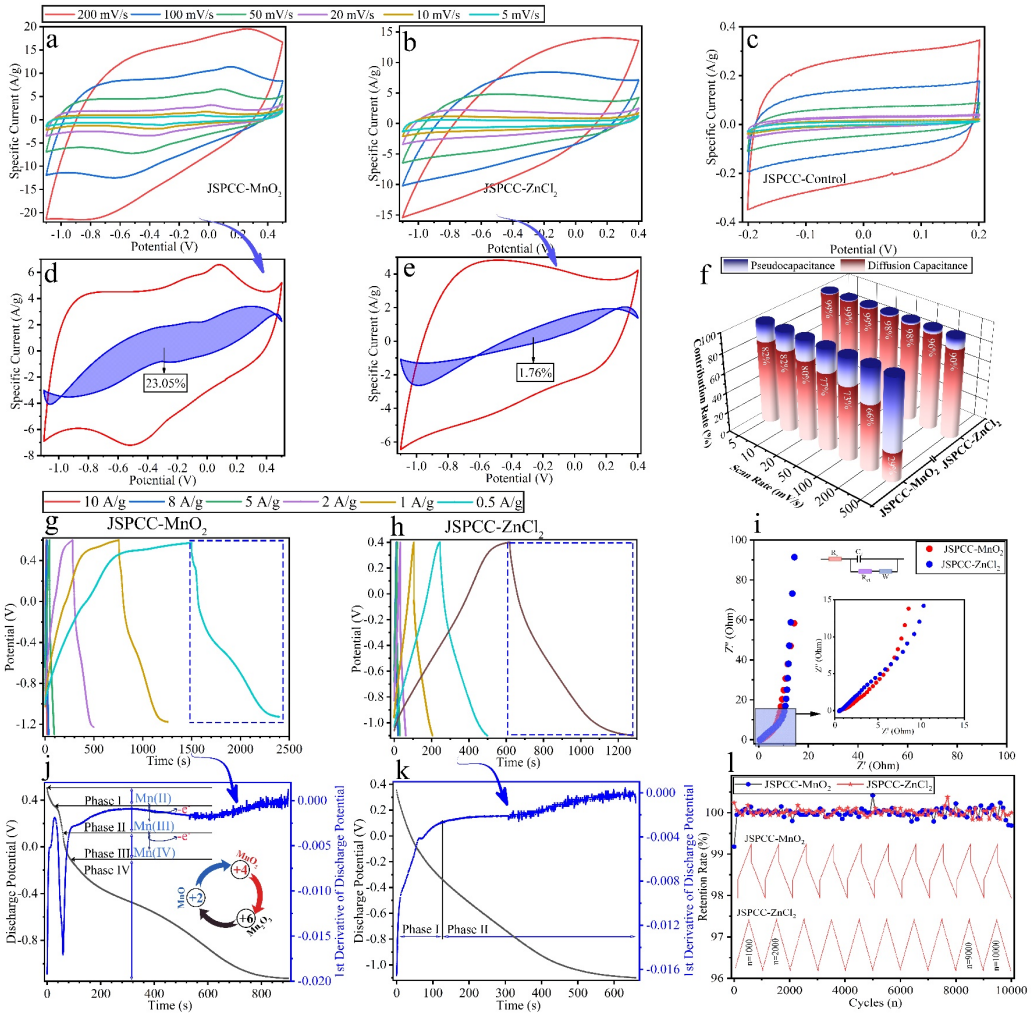

638

639 Fig. 2 Overview of electrochemical properties of composites. The CV curves and the

640 pseudo-capacitive contribution with the increasing of scanning rates (5, 10, 20, 50, 100,

641 200 mV/s). a: CV curves of JSPCC-MnO_2; b: the pseudo-capacitance vs total

642 capacitance profile of JSPCC-MnO_2 at 5 mV/s; c: curve of JSPCC-$ZnCl_2$; d: the

643 pseudo-capacitance vs total capacitance profile of JSPCC-$ZnCl_2$ at 5 mV/s; e: curves

644 of JSPCC-Control; f: the pseudo-capacitive contribution at different scanning rates;

645 GCD, EIS (k) and cyclic stability (l) of electrode materials. GCD curves of electrode

646 materials at gradient current densities and the first derivative of the discharge voltage

647 to time at 0.5 A/g (g and h: JSPCC-MnO_2, i and j: JSPCC-$ZnCl_2$).

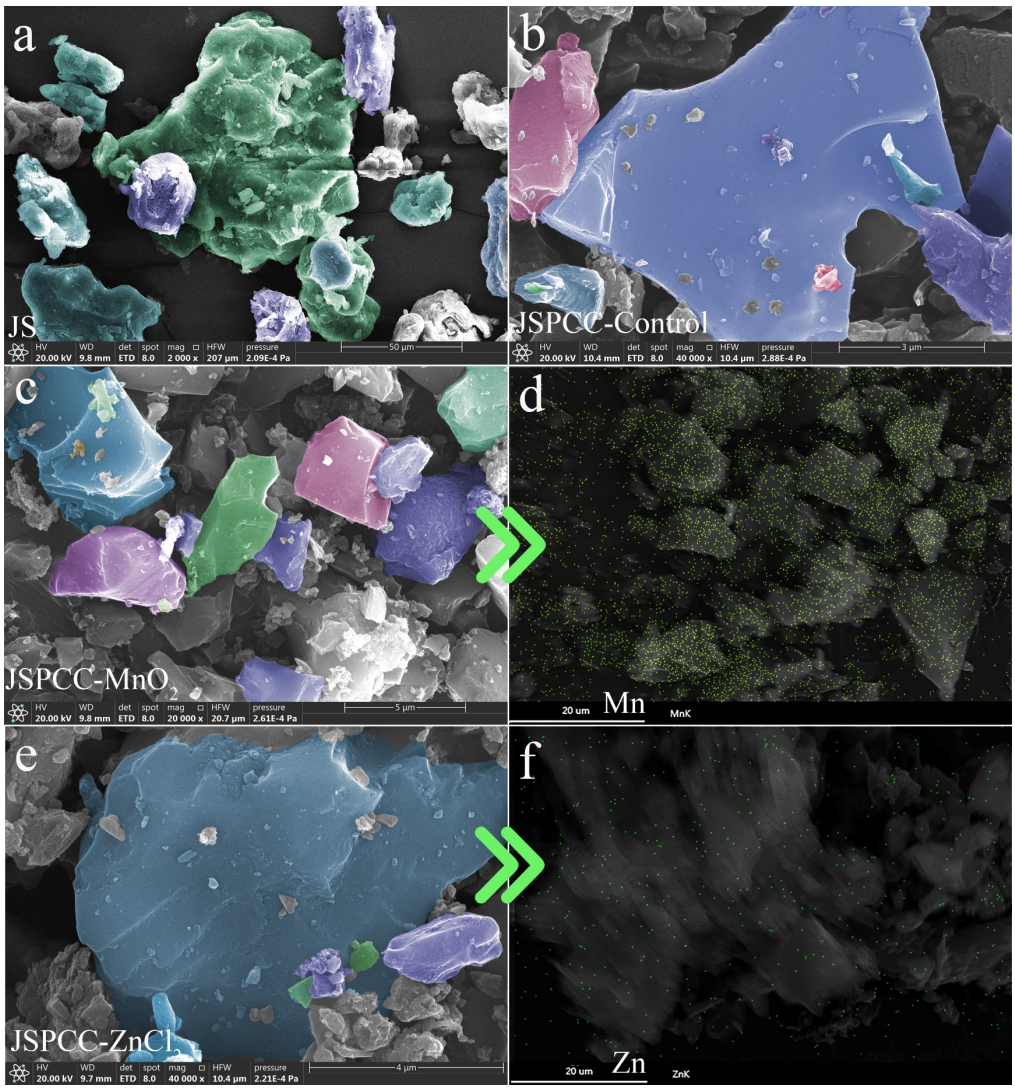

Fig. 3 Surface morphology and element distribution of porous carbon composites from SEM. a: JS; b: JSPCC-Control; c and d: JSPCC-MnO_2; e and f: JSPCC-$ZnCl_2$.

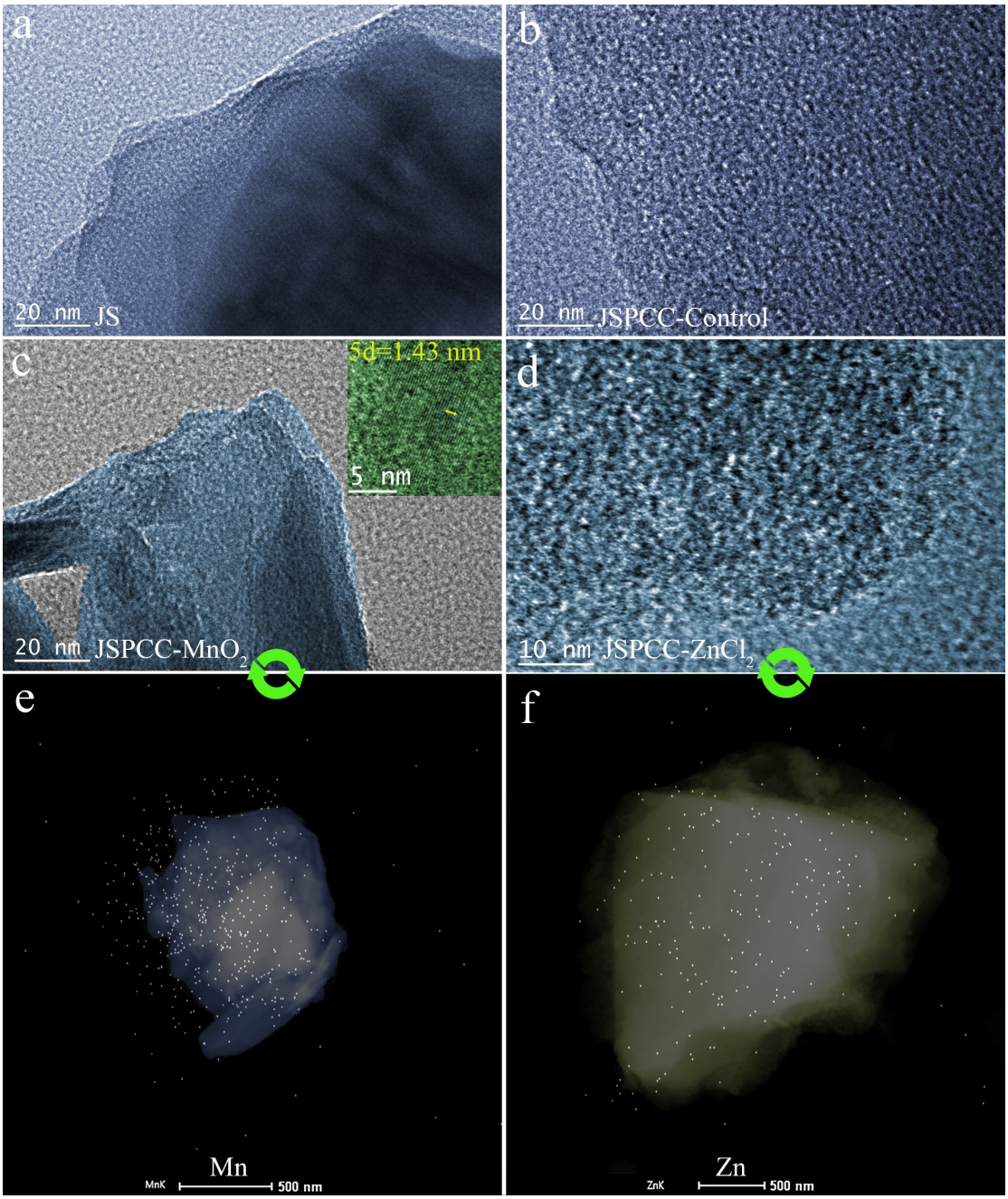

653

654 Fig. 4 TEM morphology and element distribution of porous carbon composites (Mn or

655 Zn element). a: JS; b: JSPCC-Control; c and e: JSPCC-MnO_2; d and f: JSPCC-$ZnCl_2$.

656

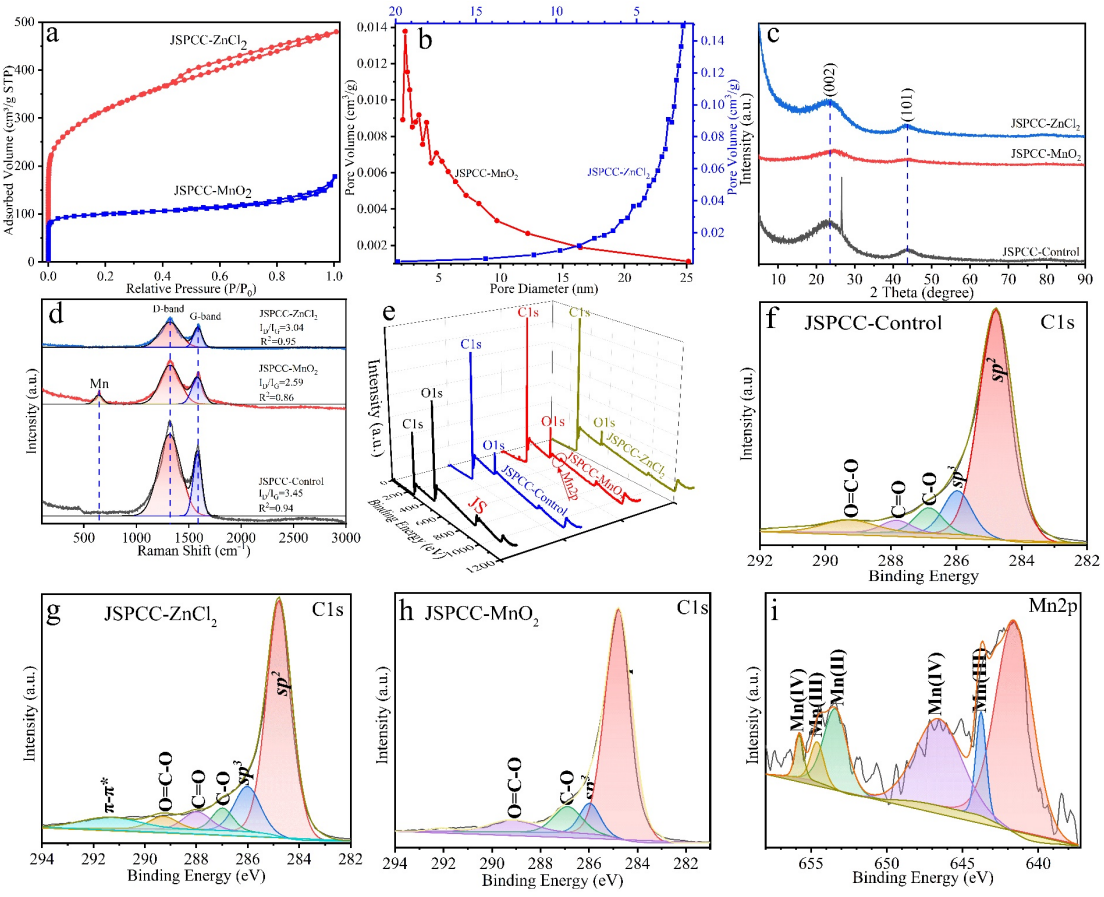

657

658 Fig. 5 Physicochemical properties of porous carbon composites. N_2 adsorption-

659 desorption isotherm (a), pore size distribution of porous carbon composites (b), XRD

660 (c), Raman (d), XPS survey spectra (e), Mn2p (i), and high-resolution C1s spectrum (f:

661 JSPCC-Control; g: JSPCC-$ZnCl_2$; h: JSPCC-MnO_2).

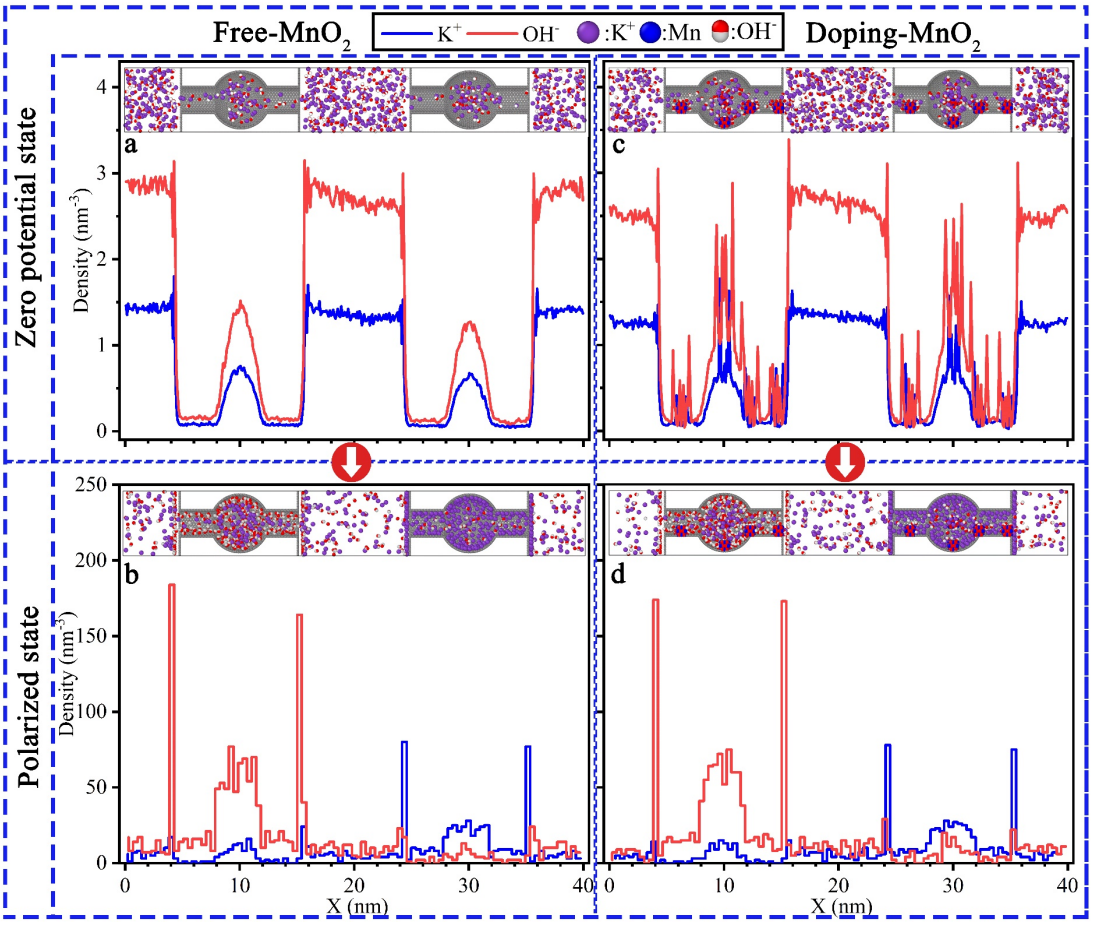

Fig. 6 The one-dimensional distribution of electrolyte ions in the nanoscale at the zero-potential state and the polarization state. a and b: Free-MnO_2 (a: Zero potential state, b: Polarized state). c and d: Doping-MnO_2 (c: Zero potential state, d: Polarized state).

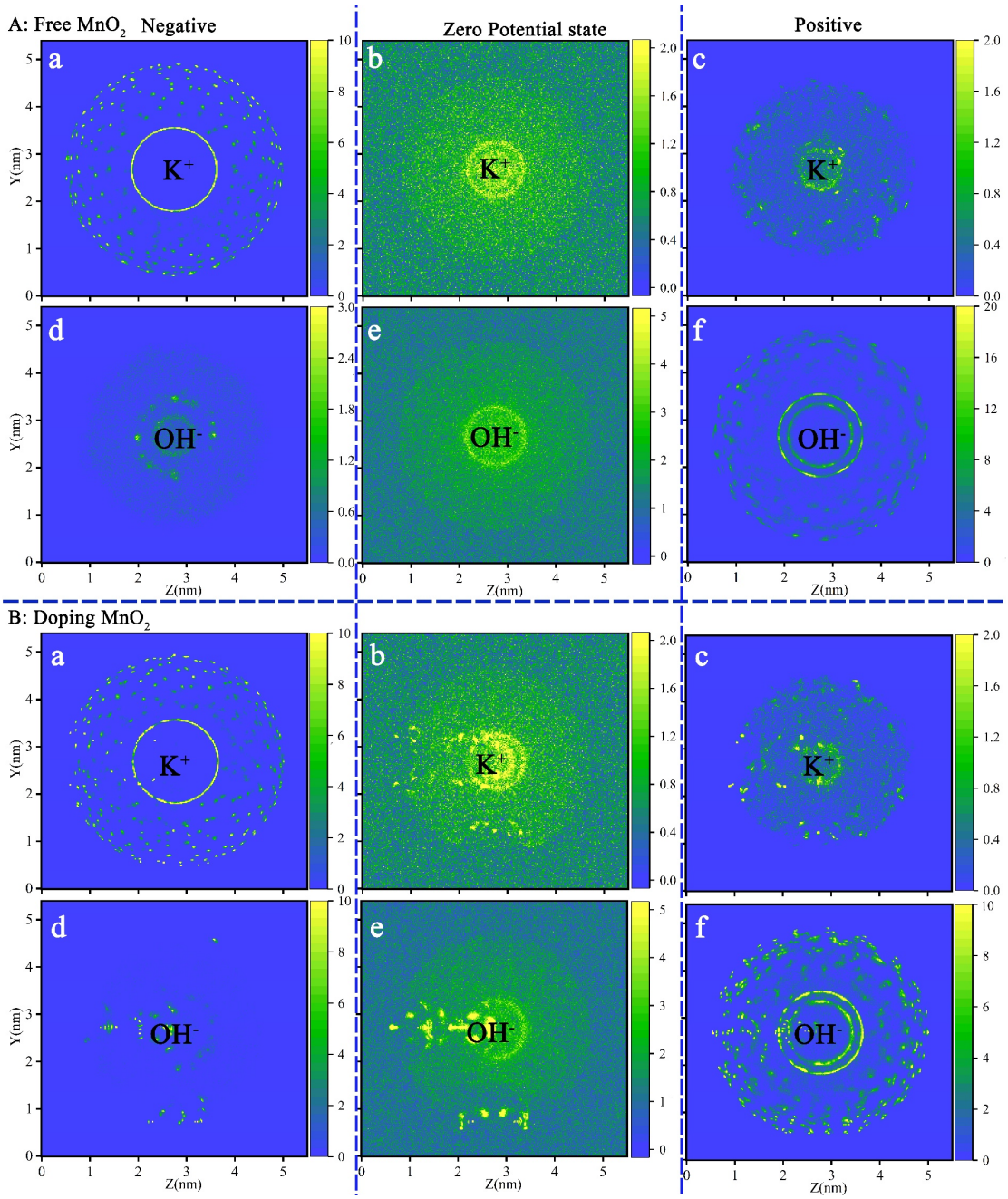

Fig. 7 The two-dimensional distributions of anions (OH^-) and cations (K^+) in the nanoscale at the zero-potential and polarization states. A: Free-MnO2; B: Doping MnO_2. a, b, and c represent the two-dimensional distribution of cations (K^+) in negative, zero potential and positive states, respectively. d, e, and f represent the two-dimensional of anions (OH^-) in negative, zero potential and positive states, respectively.

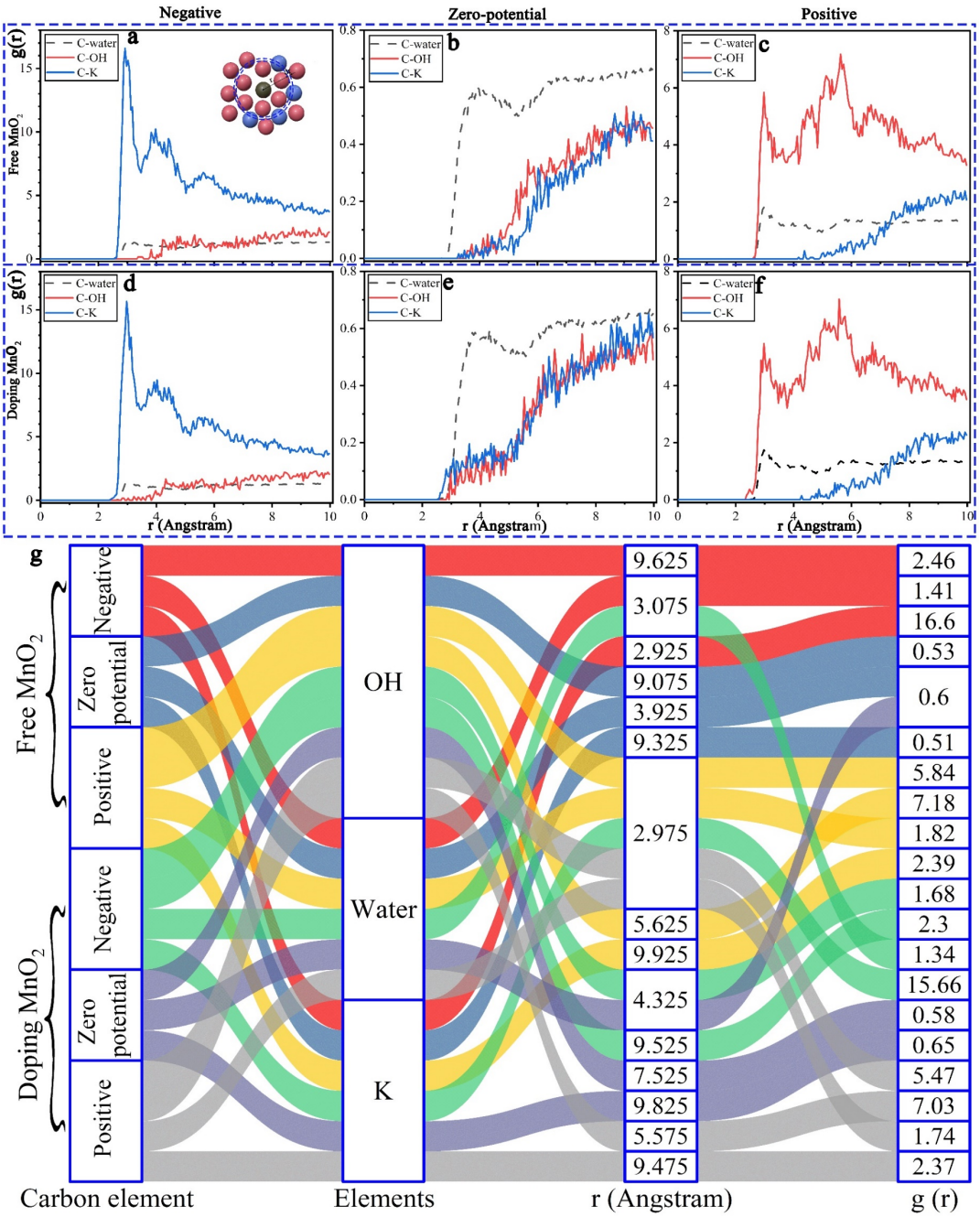

Fig. 8 The RDF diagram of C-K, C-OH, and C-water at zero-potential and polarization states. a, b, and c represent negative, zero potential and positive states at Free-MnO_2. d, e, and f represent negative, zero potential and positive states at Doping-MnO2. g refers to the peak position and corresponding intensity of the RDF diagram of C-K, C-OH, and C-water under different conditions